# CONVECTIVE HEAT TRANSFER IN NANOFLUIDS

by

STEVEN SCHRAUDNER
B.S. (Computer Science), Purdue University, 2002
B.S. (Mathematics), Purdue University, 2002
M.S. (Computer Science), Indiana University-Purdue University-Indianapolis, 2007

A thesis submitted in partial fulfillment of the requirements
for the degree of Master of Science
in the Department of Mathematics
in the College of Sciences
at the University of Central Florida
Orlando, Florida

Spring Term
2012

# ABSTRACT

In recent years, the study of fluid flow with nanoparticles in base fluids has attracted the attention of several researchers due to its various applications to science and engineering problems. Recent investigations on convective heat transfer in nanofluids indicate that the suspended nanoparticles markedly change the transport properties and thereby the heat transfer characteristics. Convection in saturated porous media with nanofluids is also an area of growing interest. In this thesis, we study the effects of radiation on the heat and mass transfer characteristics of nanofluid flows over solid surfaces.

In Chapter 2, an investigation is made into the effects of radiation on mixed convection over a wedge embedded in a saturated porous medium with nanofluids, while in Chapter 3 results are presented for the effects of radiation on convection heat transfer about a cone embedded in a saturated porous medium with nanofluids.

The resulting governing equations are non-dimensionalized and transformed into a non-similar form and then solved by Keller box method. A comparison is made with the available results in the literature, and the results are found to be in very good agreement. The numerical results for the velocity, temperature, volume fraction, the local Nusselt number and the Sherwood number are presented graphically. The salient features of the results are analyzed and discussed for several sets of values of the pertinent parameters. Also, the effects of the Rosseland diffusion and the Brownian motion are discussed.

This thesis is dedicated to my family, especially my parents and sister, whose love and support have made all things possible.

# ACKNOWLEDGMENTS

I would like to sincerely thank my advisor, Dr. Kuppalapalle Vajravelu, for his guidance, patience, and encouragement throughout my academic career and especially while I prepared this thesis. I would also like to thank my thesis committee members, Dr. Ram Mohapatra and Dr. David Rollins, for their suggestions and encouragement during the course of this work. Finally, I would like to express my gratitude to Dr. Ali J. Chamkha, Dr. S. Abbasbandy, and Dr. A. M. Rashad for reviewing and making valuable suggestions which led to definite improvements in the thesis.

# TABLE OF CONTENTS

# LIST OF FIGURES

# LIST OF TABLES

# LIST OF SYMBOLS

| *Symbol* | *Quantity* |
|---|---|
| | Letter Symbols |
| C | nano-particle volume fraction |
| $D_B$ | Brownian diffusion coefficient |
| $D_T$ | thermophoretic diffusion coefficient |
| g | acceleration of gravity |
| k | thermal conductivity |
| K | permeability of porous medium |
| $Pe_x$ | local Peclet number |
| $Ra_x$ | local Rayleigh number |
| T | temperature |
| u | velocity component in the *x*-direction |
| v | velocity component in the *y*-direction |
| | Greek Letters |
| $\beta$ | volumentric expansion coefficient of fluid |
| $\gamma$ | half-cone angle |
| $\rho_f$ | fluid density |
| $\rho_p$ | nano-particle mass density |
| $\sigma$ | Stefan-Boltzmann constant |
| $\sigma_s$ | scattering coefficient |
| $\varphi$ | half-wedge angle |

# CHAPTER 1
# INTRODUCTION

## 1.1 Background

Humans have been fascinated with heat and energy since the discovery of fire, but scientists and mathematicians have been especially interested with the prediction and modeling of heat transfer since the Industrial Revolution. With the ability to convert heat and energy into power (using inventions like the steam- and combustion-engine), it became clear that fully understanding exactly how heat transfer takes place from one medium to another was the key to conserving energy and making the most efficient devices and processes possible. It was known that there were three main types of heat transfer: conduction, convection, and radiation. Conduction is the direct transfer of heat between adjacent particles, and it can be thought of as heat transfer on a microscopic level. Convection refers to the flow of heat through a liquid or gas along with the flow of the mass itself. Therefore convection is typically thought of as a large-scale level of heat transfer. Finally, radiation is the transfer of energy (and thus heat) directly through electromagnetic waves.

Of the three types of heat transfer, convection was the most difficult to model because it required a complete understanding of the flow of fluids. Unfortunately the large number of interacting forces and physical characteristics involved in fluid flow proved to be too complex for initial mathematical models to be accurate. Specifically, if friction forces were added to the Newtonian motion equations, the system had no known analytical solutions and hence could only be solved numerically (which was especially tedious and unhelpful before the advent of

computers). Neglecting friction in Newtonian motion equations allowed for analytical solutions, but the predicted results did not align with actual results seen in practice. Scientists could not understand why the neglected friction forces, which seemed small in comparison to the gravity and pressure forces (especially in common fluids like air and water), would cause such large discrepancies in their calculations. A breakthrough was finally made by Prandtl in the early 1900s when he noticed that one could ignore the friction forces except on the fluid closest to the system surfaces. In other words, a mass of fluid could be considered two separate parts: an inner area where friction forces could be ignored, and the layer of fluid touching the system boundaries where friction forces had to be included. Since the boundary layer was typically much smaller than the inner area, the ensuing equations were simplified and could be solved analytically. Using Prandtl's boundary layer theory, scientists were finally able to accurately predict the flow of fluids and, therefore, convective heat transfer.

Unfortunately for those seeking to improve energy efficiency, a mathematical model for heat flow did not solve all of their problems. Another common issue was the difficulty in combining conduction and convection. This was because materials that conducted heat well (such as metals) did not flow very well, and materials that flowed well (such as water and air) did not conduct heat very well. Heating metals into liquid form was one option, but it was not considered very practical because of the large amounts of energy required to reach the necessary temperatures. A different solution, first proposed by Maxwell in 1873, was to add small particles of highly-conductive solids to regular liquids like water and alcohol. For over a century it was only possible to produce these particles in diameters as small as millimeters and micrometers. Unfortunately, particles at those sizes tended to settle out of the fluids, caused erosion in their

containers, clogged very small passages, and caused considerable pressure drops in the fluids. However, in the past few decades advances in nanotechnology have allowed production of particles measured in terms of nanometers, and solid-liquid solutions with these particles have come to be known as nanofluids. Although research is still ongoing, it appears that properly prepared nanofluids do not have the adverse effects associated with their larger-particle counterparts. It has also been shown that nanofluids do indeed provide much better thermal conductivity compared to regular fluids. Because they have such promise and potential, the study of heat transfer in nanofluids has increased dramatically in recent years and shows no signs of slowing down.

For those wishing to learn more about boundary layer theory, a good introduction can be found in the textbook on fluid mechanics by Fox and McDonald [1], while the classic textbook by Schlichting [2] dealing entirely with boundary layer theory is perfect for those looking for a deep, comprehensive understanding of the subject. In addition, the textbook by Pop and Ingham [3] is an excellent resource for mathematical models dealing specifically with convective heat transfer in porous media.

## 1.2 Purpose of Study

The enhanced heat transfer properties of nanofluids have been studied extensively, and several relations have been noted. Masuda et al. [4] were the first to examine the thermal conductivity of nanofluids and found that conductivity increased linearly with particle volume fraction. Lee et al. [5] also found a linear dependence between particle volume fraction and conductivity, but more importantly they also noticed that using particle materials with better

thermal conductivity did not necessarily always lead to nanofluids with better thermal conductivity. The authors speculated that what was more important was how the particles clustered and observed that smaller clusters were one reason for the enhanced properties of nanofluids. Using ultrasonic vibrations, Hong et al. [6] were able to vary cluster sizes in nanofluids over time and also concluded that smaller clusters led to better thermal conductivity. Similarly, Chopkar et al. [7] examined nanofluids composed of particles of identical materials but different sizes and determined that thermal conductivity was inversely related to particle size itself. Finally, Li and Peterson [8] noted that thermal conductivity increases as the nanofluid temperature rises, and Li et al. [9] pointed out that the change in temperature affected the Brownian motion and clustering of nanoparticles. In fact, since smaller particles, smaller clusters, and higher temperatures lead to increased Brownian motion of particles, many have surmised that it is this Brownian motion in nanofluids that gives them the enhanced heat transfer properties: Xuan et al. [10] have shown that the increased heat transfer rate is at least partially due to random particle motion.

The study of heat transfer through convection has been very active in the past century, but there has also been a specific interest in convection around and through shapes like spheres, cones, and wedges. The flow of heat around these objects has applications in many fields including the design of spacecraft, nuclear reactors, and many types of transformers and generators. Takhar et al. [11] studied the mathematical solutions of free convection flow of gases around a vertical cone, while Alam et al. [12] performed similar research on free convection flow around a permeable vertical cone. Pop et al. [13] examined the entire range of mixed convection (from free convection to forced convection) about a vertical cone. Vajravelu

and Nayfeh [14] investigated free convection in heat-generating fluids around both cones and wedges. The last few decades have also shown a major increase in the research of convective heat transfer through porous media. This is because it is directly applicable to topics such as nuclear waste storage, ground-water pollution, chemical separation processes, and many other areas of interest. In the past few years, this research has also considered the special case where the porous media is saturated with nanofluids. Chamkha et al. [15] studied free convection around a sphere embedded in a nanolfuid-filled porous medium, while Gorla et al. [16] analyzed mixed convection past a wedge embedded in a porous medium saturated with nanofluids.

Another important area of study is the effect of radiation on convective heat transfer. These effects are more pronounced in cases of extremely high temperatures and are therefore very applicable in fields such as space technology and geothermal engineering. Bakier [17] analyzed the effect of radiation on mixed convection around a vertical flat plate embedded in a porous medium. Similarly, Kumari and Nath [18] presented research on the effect of radiation on mixed convection about a non-isothermal horizontal plate embedded in a porous medium. Finally, of special interest to the results presented in this thesis was the research of Yih [19] who studied the effect of radiation on mixed convection over an isothermal wedge embedded in porous media.

Unfortunately, to date there has been little research about the effects of radiation on mixed convection in porous media specifically saturated with nanofluids. Motivated by this need and the aforementioned studies, an investigation was made into the effects of radiation on mixed

convection over cones and wedges in nanofluid-filled porous media while specifically taking Brownian motion into account.

### 1.3 Thesis Overview

In Chapter 2, results are presented for the effects of thermal radiation on laminar, steady mixed convection flow about a cone which is embedded in a porous medium saturated with an incompressible nanofluid. The cone is assumed to be isothermal and vertically-aligned, while the porous medium is assumed to be uniform and in thermal equilibrium with the nanofluid.

In Chapter 3, an investigation is made into the effects of thermal radiation on laminar, steady mixed convection flow about an isothermal, vertically-aligned wedge which is embedded in a porous medium saturated with an incompressible nanofluid. Once again, the porous medium is assumed to be uniform and in thermal equilibrium with the nanofluid.

In Chapters 2 and 3, the equations used to model the systems account for both Rosseland diffusion and Brownian motion, and they are solved numerically using the Keller box method. Solutions are obtained from entirely free convection flow all the way to entirely forced convection flow and are compared with published results. Nusselt and Sherwood numbers are also obtained numerically across the full range of convection and are studied and discussed.

# CHAPTER 2
# MIXED CONVECTION OVER A WEDGE EMBEDDED IN A POROUS MEDIUM FILLED WITH A NANOFLUID

## 2.1 Introduction

In this chapter we will provide the results of Chamkha et al. [20], where consideration is given to the effects of thermal radiation on steady, laminar, mixed convection boundary layer flow over an isothermal vertical wedge embedded in a porous medium saturated with a nanofluid. Equations governing the system that account for Brownian motion and thermophoresis (using Rosseland diffusion approximation) are presented. These equations are solved numerically using the Keller box method. Results, including the local Nusselt and Sherwood numbers, are computed along the entire range of convection and for varying physical values. Comparisons are made with available results, and good agreement is found.

## 2.2 Analysis

Consider the problem of a vertically-aligned wedge whose tip resides at $x = 0$, $y = 0$ and whose wedge angle is given by $2\varphi$ (Figure 2.1). The uniform wall temperature of the wedge $T_w$ is higher than the ambient temperature $T_\infty$, and the uniform nano-particle volume fraction of the wedge $C_w$ is higher than the ambient nano-particle volume fraction $C_\infty$. It is assumed that all fluid properties are constant, and the flow over the wedge is two-dimensional, laminar, steady, and incompressible. The porous medium is assumed to be uniform and isotropic. It is also assumed that the porous medium is in local thermal equilibrium with the fluid.

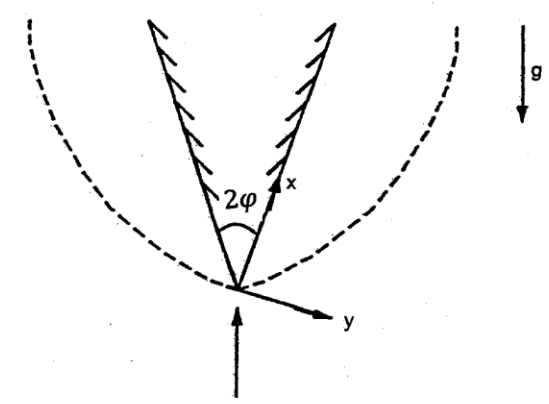


**Figure 0.1**
**A Sketch of the Physical Model**

Let $u$ and $v$ be the velocity components in the $x$ and $y$ direction, respectively, and then the continuity equation is

$$\frac{\partial u}{\partial x}+\frac{\partial v}{\partial y}=0 \tag{1}$$

because the flow is incompressible. The Darcy model combined with the Boussinesq approximation also gives the momentum equation

$$\frac{\partial u}{\partial y}=\frac{(1-C_\infty)\rho_{f\infty}\beta gK}{\mu}\frac{\partial T}{\partial y}-\frac{(\rho_p-\rho_{f\infty})gK}{\mu}\frac{\partial C}{\partial y}, \tag{2}$$

where $T$ is the temperature, $C$ is the nano-particle volume fraction, $K$ is the permeability of the porous medium, $\beta$ is the volumetric expansion coefficient of the nanofluid, $g$ is the gravitational acceleration constant, and $\mu$, $\rho_{f\infty}$ and $\rho_p$ are the fluid viscosity, fluid density and the nano-particle mass density, respectively. There is also the energy equation

$$u\frac{\partial T}{\partial x}+v\frac{\partial T}{\partial y}=\alpha_e\frac{\partial^2 T}{\partial y^2}+\tau\left[D_B\frac{\partial C}{\partial y}\frac{\partial T}{\partial y}+\left(\frac{D_T}{T_\infty}\right)\left(\frac{\partial T}{\partial y}\right)^2\right] + \frac{16\sigma}{3(a_r+\sigma_s)(c_p\rho)_f}\frac{\partial}{\partial y}\left(T^3\frac{\partial T}{\partial y}\right), \tag{3}$$

where $k$ is the thermal conductivity, $(\rho c)_f$ is the heat capacity of the fluid, $(\rho c)_p$ is the effective heat capacity of the nano-particle material, $\alpha_e = k/(\rho c)_f$ is the thermal diffusivity of the porous medium, $\tau = (\rho c)_p/(\rho c)_f$ is the ratio of heat capacities, $\sigma$ is the Stefan-Boltzmann constant, $\sigma_s$ is the scattering coefficient, $a_r$ is the Rosseland mean extinction coefficient, and $D_B$ and $D_T$ are the Brownian diffusion coefficient and thermophoretic diffusion coefficient, respectively. Note that the last term on the right side of the energy transfer equation (3) is the thermal radiation heat flux and is approximated using the Roseland diffusion equation. Further, the mass transfer equation is given by

$$u\frac{\partial C}{\partial x}+v\frac{\partial C}{\partial y}=D_B\frac{\partial^2 C}{\partial y^2}+\left(\frac{D_T}{T_\infty}\right)\frac{\partial^2 T}{\partial y^2}. \tag{4}$$

Finally, the appropriate boundary conditions suggested by the physics of the problem are

$$y=0:\quad v(x,0)=0,\quad T=T_w,\quad C=C_w, \tag{5a}$$

$$y\to\infty:\quad u=U_\infty,\quad T=T_\infty,\quad C=C_\infty, \tag{5b}$$

where $U_\infty$, is the free stream velocity.

For the given system of equations it is actually convenient to transform them into a non-similar dimensionless form which can be studied as an initial-value problem. This is done by introducing the stream function: $u=\partial\psi/\partial y, v=-\partial\psi/\partial x$ and the variables

$$\eta = \frac{y}{x}(Pe_x{}^{1/2})\chi^{-1},\ \chi = \left(1+\left(\frac{Ra_x}{Pe_x}\right)^{1/2}\right)^{-1}\ \psi = \alpha_e(Pe_x{}^{1/2})\chi^{-1}f\ (\chi,\eta),\ \theta = \frac{T-T_\infty}{T_w-T_\infty},$$

$$\phi = \frac{C-C_\infty}{C_w-C_\infty},\quad \lambda = \frac{\varphi}{\pi-\varphi},\quad U_\infty = Bx^{\lambda},\quad Pe_x = U_\infty x/\alpha_e,$$

$$Ra_x = \left\{(1-C_\infty)\rho_{f\infty}g\beta_T K(T_w-T_\infty)x/\mu\alpha_e\right\}, \tag{6}$$

where $Pe_x$ is the local Peclet number, $Ra_x$ is the modified Rayleigh number, $a$ is the free stream velocity constant, and $\lambda$ is the free stream velocity exponent. Using the expressions above, one can transform equations (1) - (4) and the boundary conditions (5) into

$$f'' = (1-\chi)^2(\theta' - Nr\phi'), \tag{7}$$

$$\begin{aligned}&\theta'' + \frac{1}{2}(1+\lambda\chi)f\theta' + Nb\phi'\theta' + Nt\theta'^2\\ &+\frac{4R_d}{3}\left\{\theta'\left[(H-1)\theta+1\right]^3\right\}' = \frac{\lambda}{2}\chi(1-\chi)(f'\frac{\partial\theta}{\partial\chi} - \theta'\frac{\partial f}{\partial\chi}),\end{aligned} \tag{8}$$

$$\phi'' + \frac{Le}{2}(1+\lambda\chi)f\ \phi' + \frac{Nt}{Nb}\theta'' = \frac{Le}{2}\lambda\chi(1-\chi)(f'\frac{\partial\phi}{\partial\chi} - \phi'\frac{\partial f}{\partial\chi}), \tag{9}$$

$$(1+\lambda\chi)f\ (\chi,0) - \lambda\chi(1-\chi)\frac{\partial f}{\partial\chi}(\chi,0) = 0,\ \ \theta(\chi,0) = 1,\quad \phi(\chi,0) = 1, \tag{10a}$$

$$f'(\chi,\infty) = \chi^2,\ \ \theta(\chi,\infty) = 0,\quad \phi(\chi,\infty) = 0, \tag{10b}$$

where $Le = \frac{\alpha_e}{D_B}$, $Nr = \frac{(\rho_p - \rho_{f\infty})(C_w - C_\infty)}{(1-C_\infty)\rho_{f\infty}\beta(T_w - T_\infty)}$, $Nb = \frac{\varepsilon(\rho c)_p D_B(C_w - C_\infty)}{(\rho c)_f\ \alpha_e}$,

$$Nt = \frac{\varepsilon(\rho c)_p D_T(T_w - T_\infty)}{(\rho c)_f\ \alpha_e T_\infty}, R_d = 4\sigma T_\infty^3/\left[k\left(a_r + \sigma_s\right)\right], H = T_w/T_\infty\ , \tag{11}$$

are the Lewis number, buoyancy ratio, Brownian motion parameter, thermophoresis parameter,

conduction-radiation parameter and the surface temperature excess ratio, respectively. It is important to note that $Pe_x = 0$, which represents pure free convection, corresponds to the $\chi$ value of 0, while $Ra_x = 0$, which represents pure forced convection, corresponds to the $\chi$ value of 1. Thus, varying $\chi$ between 0 and 1 allows computations over the entire range of mixed convection.

Finally, it is useful to define the local Nusselt number $Nu_x$ and the local Sherwood number $Sh_x$ with the equations

$$\frac{Nu_x}{Ra_x^{1/2} + Pe_x^{1/2}} = -\theta'(\chi, 0)\left(1 + \frac{4R_d H^3}{3}\right), \tag{12}$$

$$\frac{Sh_x}{Ra_x^{1/2} + Pe_x^{1/2}} = -\phi'(\chi, 0) \tag{13}$$

The local Nusselt number is a dimensionless ratio of convective heat transfer to conductive heat transfer across a boundary. A ratio close to 1 typically indicates laminar flow, whereas much higher values represent more active flow that may or may not be turbulent. Similarly, the local Sherwood number is a dimensionless ratio of convective mass transfer to diffusive mass transfer.

### 2.3 Numerical Methods

The system of non-linear partial differential equations (7), (8) and (9) along with the mixed boundary conditions (10) are solved numerically, and the Keller box method is used. This method converts the system into nonlinear finite difference equations by using midpoints over rectangles in the graph, then linearizes them with Newton's method and solves the resulting equations with factorization [21]. In this case, the computations were carried out with $\Delta\chi = 0.01$ and $\Delta\eta = 0.01$ (uniform grids). It was found that a value of $\eta_\infty = 50$ was sufficient enough to

obtain a desired accuracy of $|\theta'(0)| < 10^{-5}$. First, the buoyancy ratio $N_r$, the Brownian motion parameter $N_b$, the thermophoresis parameter $N_t$, and the radiation–conduction parameter $R_d$ were set to zero in order to compare results to those published by Hsieh et al. [22] and Yih [19]. There was an excellent agreement, and these results are presented in Table 2.1.

**Table 0.1**
**Comparison of Results with Published Results for the Full Range of Convection**

| | Hsieh et al. [22] | Yih [19] | | | Present results | | |
|---|---|---|---|---|---|---|---|
| $\chi$ | $\lambda$=0 | $\lambda$=0 | $\lambda$=1/3 | $\lambda$=1 | $\lambda$=0 | $\lambda$=1/3 | $\lambda$=1 |
| 1.0 | 0.5642 | 0.5642 | 0.6515 | 0.7979 | 0.5642 | 0.6516 | 0.7979 |
| 0.9 | 0.5098 | 0.5097 | 0.5878 | 0.7181 | 0.5098 | 0.5879 | 0.7181 |
| 0.8 | 0.4603 | 0.4602 | 0.5278 | 0.6385 | 0.4602 | 0.5280 | 0.6385 |
| 0.7 | 0.4174 | 0.4173 | 0.4731 | 0.5599 | 0.4173 | 0.4732 | 0.5599 |
| 0.6 | 0.3832 | 0.3832 | 0.4261 | 0.4854 | 0.3832 | 0.4261 | 0.4854 |
| 0.5 | 0.3603 | 0.3603 | 0.3900 | 0.4227 | 0.3603 | 0.3901 | 0.4227 |
| 0.4 | 0.3506 | 0.3505 | 0.3686 | 0.3823 | 0.3506 | 0.3687 | 0.3823 |
| 0.3 | 0.3550 | 0.3550 | 0.3643 | 0.3697 | 0.3550 | 0.3643 | 0.3697 |
| 0.2 | 0.3732 | 0.3732 | 0.3769 | 0.3786 | 0.3732 | 0.3769 | 0.3786 |
| 0.1 | 0.4035 | 0.4035 | 0.4044 | 0.4049 | 0.4035 | 0.4043 | 0.4049 |
| 0.0 | 0.4438 | 0.4437 | 0.4437 | 0.4437 | 0.4437 | 0.4437 | 0.4437 |

Computations were also carried out for several sets of values of the physical parameters. The effects of these variations were examined against the velocity, temperature, and volume fraction profiles, as well as against the dimensionless Nusselt and Sherwood numbers. Figures

2.2 and 2.3 show how the Nusselt and Sherwood numbers were affected, respectively, for various values of the wedge angle $\lambda$. Note that for these cases $R_d = 3$, $H = 2$, $N_r = 0.5$, $N_b = 0.3$, $N_t = 0.1$, and $Le = 10$.

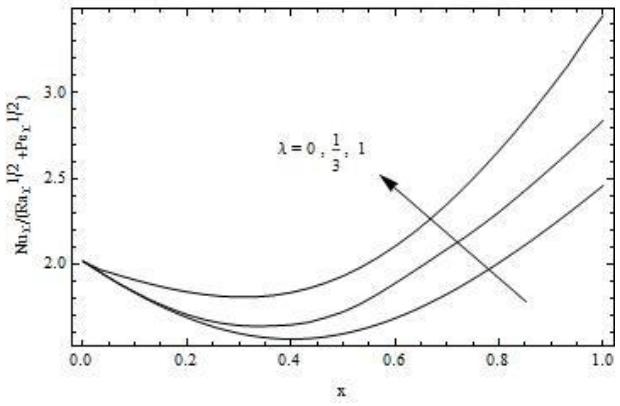


**Figure 0.2**
**The Local Nusselt Number Profile for Various Values of $\lambda$**

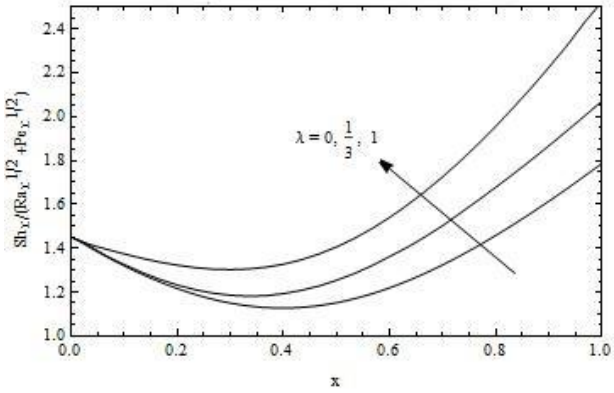


**Figure 0.3**
**The Local Sherwood Number Profile for Various Values of $\lambda$**

Figures 2.4 and 2.5 show the effects on the Nusselt and Sherwood numbers, respectively, when varying the Brownian motion parameter $N_b$. For these cases $R_d = 3$, $\lambda = 1/3$, $H = 2$, $N_r = 0.5$, $N_t = 0.1$, and $Le = 10$.

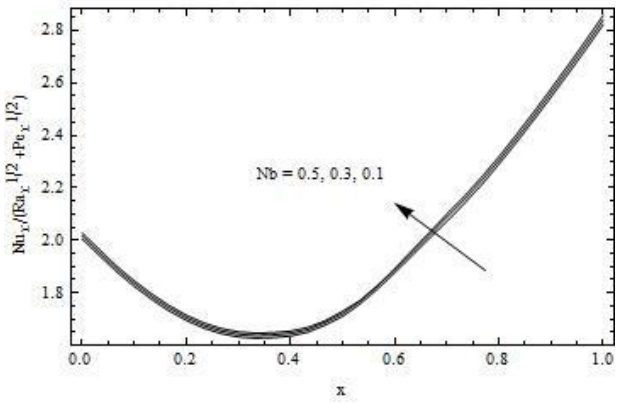


**Figure 0.4**
**The Local Nusselt Number Profile for Various Values of $N_b$**

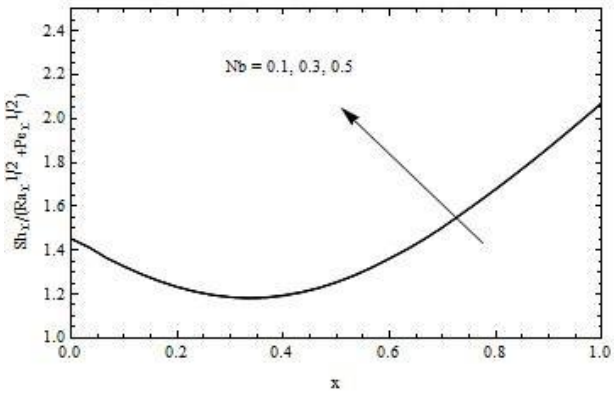


**Figure 0.5**
**The Local Sherwood Number Profile for Various Values of $N_b$**

Figures 2.6 and 2.7 show how varying the thermophoresis parameter $N_t$ affects the local Nusselt and Sherwood numbers. For these calculations, the parameters are $R_d = 3$, $\lambda = 1/3$, $H = 2$, $N_r = 0.5$, $N_b = 0.3$, and $Le = 10$.

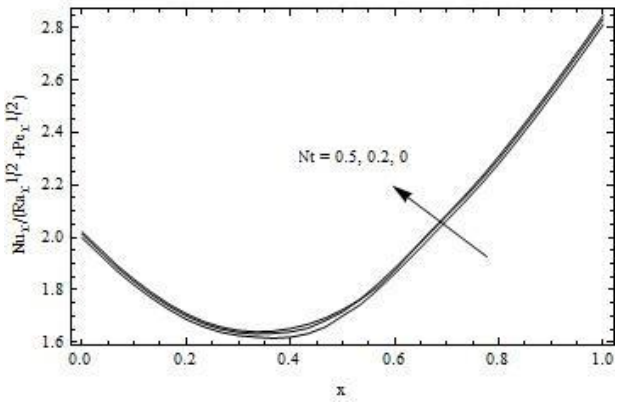


**Figure 0.6**
**The Local Nusselt Number Profile for Various Values of $N_t$**

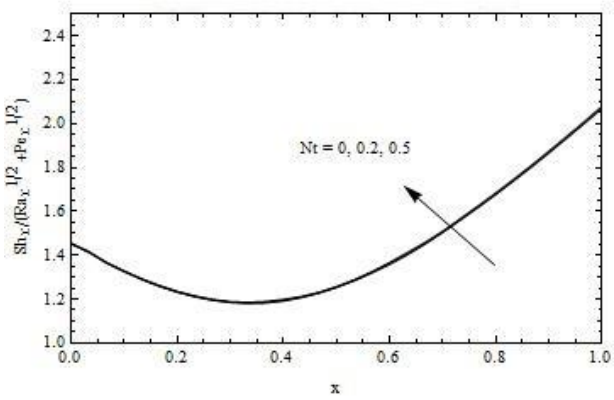


**Figure 0.7**
**The Local Sherwood Number Profile for Various Values of $N_t$**

Finally, Figures 2.8 and 2.9 show how changes in the radiation–conduction parameter $R_d$ affect the local Nusselt and Sherwood numbers. In these scenarios, $\lambda = 1/3$, $H = 2$, $N_r = 0.5$, $N_b = 0.3$, $N_t = 0.1$, and $Le = 10$.

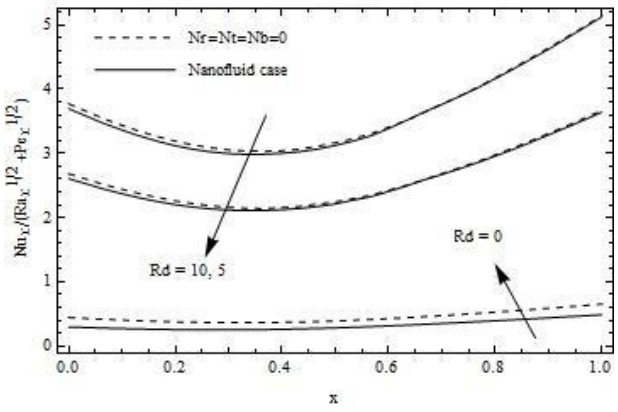


**Figure 0.8**
**The Local Nusselt Number Profile for Various Values of $R_d$**

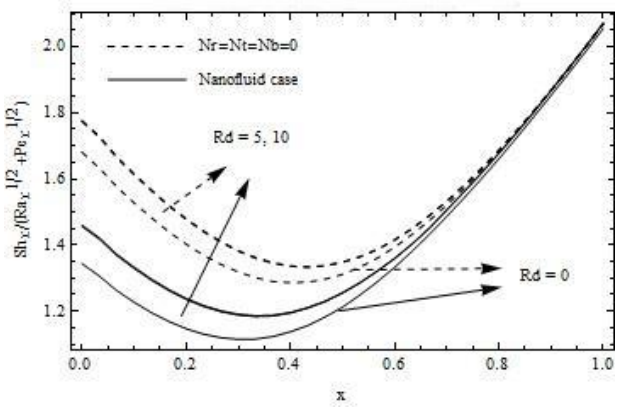


**Figure 0.9**
**The Local Sherwood Number Profile for Various Values of $R_d$**

## 2.4 Discussion of Results

Figures 2.2 and 2.3 show that the local Nusselt and local Sherwood numbers increase as the wedge angle $\lambda$ increases; indicating the enhanced heat and mass transfer. This makes sense because as the wedge angle $\lambda$ increases and the wedge becomes "flatter" and less of an obstruction, one expects mass and heat transfer to increase. Figures 2.4 and 2.5 show that

increasing $N_b$ also shows enhancements in the local Nusselt and local Sherwood numbers, although it appears that this Brownian motion parameter does not have much of an effect. Figures 2.6 and 2.7 show how changing the thermophoresis parameter affects the local Nusselt and local Sherwood numbers. Since an increase in $N_t$ causes the temperature and volume fraction to increase, the local Nusselt number increased while the local Sherwood number decreased. Finally, the effects of the radiation-conduction parameter $R_d$ on the local Nusselt number and local Sherwood number are shown in figures 2.8 and 2.9. Figure 2.8 plots the mixed convection parameter $\chi$ (over the entire range from 0 to 1) against the local Nusselt number for both Newtonian fluids and nanofluids using several different values for $R_d$, while figure 2.9 shows the same graph for the local Sherwood number. For $\chi = 0$ (pure free convection), it is apparent that increasing $R_d$ causes both the local Nusselt and local Sherwood number to increase. The figures also show that the local Nusselt number is more affected by $R_d$ than the local Sherwood number, which can be attributed to the fact that the local Nusselt number is more sensitive to $R_d$ and the suface temperature excess ratio $H$. Finally, it can also be seen that as $\chi$ approaches 1 (representing pure forced convection), the flow no longer depends on the thermal and volume fraction buoyancy effects, and hence the local Sherwood number no longer depends on $R_d$.

Overall, the local Nusselt number was found to increase whenever the wedge angle, Brownian motion, thermophoresis, or radiation-conduction parameters were increased. The local Sherwood number also increased as the wedge angle, Brownian motion, and radiation-conduction parameters were increased, but it actually decreased when the thermophoresis parameter was increased. Another observation was that the local Nusselt number and local Sherwood number tended to decrease initially when moving away from pure free convection, but

they eventually reached minimum values somewhere in the mixed convection area and gradually increased on the way to pure forced convection. Finally, it was also noted that the effects of the radiation-conduction parameter were much stronger on the local Nusselt number than the local Sherwood number, but the opposite was true for the effects of the thermophoresis parameter.

# CHAPTER 3
# MIXED CONVECTION ABOUT A CONE EMBEDDED IN A POROUS MEDIUM FILLED WITH A NANOFLUID

## 3.1 Introduction

In this chapter we will provide the results of Chamkha et al. [23], where consideration is given to the effects of thermal radiation on steady, laminar, mixed convection boundary layer flow over an isothermal vertical cone embedded in a porous medium saturated with a nanofluid. Once again, equations governing the system that account for Brownian motion and thermophoresis (using Rosseland diffusion approximation) are presented. These equations are solved numerically using the Keller box method. Results, including the local Nusselt and Sherwood numbers, are computed along the entire range of convection and for varying physical values. Comparisons are made with available results and good agreement is found.

## 3.2 Analysis

Consider the problem of a vertically-aligned isothermal cone (Figure 3.1) whose tip resides at $x = 0$, $y = 0$ and whose wedge angle is given by $2\gamma$. As in the case with wedge in Chapter 2, the uniform wall temperature of the cone $T_w$ is higher than the ambient temperature $T_\infty$, and the uniform nano-particle volume fraction of the wedge $\phi_w$ is higher than the ambient nano-particle volume fraction $\phi_\infty$. It is assumed that all fluid properties are constant, and the flow over the cone is two-dimensional, laminar, steady, and incompressible. The porous medium is assumed to be uniform and isotropic. It is also assumed that the porous medium is in local thermal equilibrium with the fluid.

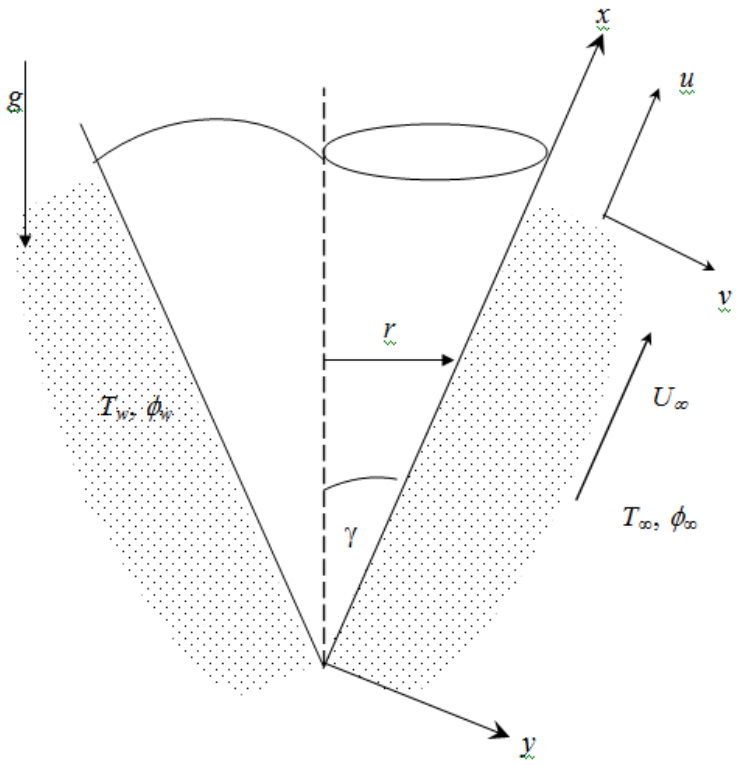


**Figure 0.1**
**A Sketch of the Physical Model**

Let *u* and *v* be the velocity components in the *x* and *y* direction, respectively, and then the continuity equation is

$$\frac{\partial(ru)}{\partial x}+\frac{\partial(rv)}{\partial y}=0, \tag{1}$$

because the flow is incompressible. The Darcy model combined with the Boussinesq approximation also gives the momentum equation

$$\frac{\partial u}{\partial y}=\frac{(1-\phi_\infty)\rho_{f\infty}\cos\gamma\beta gK}{\mu}\frac{\partial T}{\partial y}-\frac{(\rho_p-\rho_{f\infty})\cos\gamma gK}{\mu}\frac{\partial\phi}{\partial y}, \tag{2}$$

where $T$ is the temperature, $\phi$ is the nano-particle volume fraction, $K$ is the permeability of the

porous medium, $\beta$ is the volumetric expansion coefficient of the nanofluid, $g$ is the gravitational acceleration constant, and $\mu$, $\rho_{f\infty}$ and $\rho_p$ are the fluid viscosity, fluid density and the nano-particle mass density, respectively. There is also the energy transfer equation

$$u\frac{\partial T}{\partial x}+v\frac{\partial T}{\partial y}=\alpha\frac{\partial^2 T}{\partial y^2}+\tau\left[D_B\frac{\partial \phi}{\partial y}\frac{\partial T}{\partial y}+\left(\frac{D_T}{T_\infty}\right)\left(\frac{\partial T}{\partial y}\right)^2\right] + \frac{16\sigma}{3(a_r+\sigma_s)(c_p\rho)_f}\frac{\partial}{\partial y}\left(T^3\frac{\partial T}{\partial y}\right), \tag{3}$$

where $k$ is the thermal conductivity, $(\rho c)_f$ is the heat capacity of the fluid, $(\rho c)_p$ is the effective heat capacity of the nano-particle material, $\alpha = k/(\rho c)_f$ is the thermal diffusivity of the porous medium, $\tau = (\rho c)_p/(\rho c)_f$ is the ratio of heat capacities, $\sigma$ is the Stefan-Boltzmann constant, $\sigma_s$ is the scattering coefficient, $a_r$ is the Rosseland mean extinction coefficient, and $D_B$ and $D_T$ are the Brownian diffusion coefficient and thermophoretic diffusion coefficient, respectively. As in Chapter 2, note that the last term on the right side of the energy transfer equation (3) is the thermal radiation heat flux and is approximated using the Roseland diffusion equation. Further, there is the mass transfer equation

$$u\frac{\partial \phi}{\partial x}+v\frac{\partial \phi}{\partial y}=D_B\frac{\partial^2 \phi}{\partial y^2}+\left(\frac{D_T}{T_\infty}\right)\frac{\partial^2 T}{\partial y^2}. \tag{4}$$

Finally, the appropriate boundary conditions suggested by the physics of the problem are

$$y=0: \quad v(x,0)=0, \quad T=T_w, \quad \phi=\phi_w, \tag{5a}$$

$$y\to\infty: \quad u=U_\infty, \quad T=T_\infty, \quad \phi=\phi_\infty, \tag{5b}$$

where $U_\infty$, is the free stream velocity. For cone flow, $U_\infty$ is calculated using the equation

$U_\infty = Bx^m$, where $B$ is a prescribed constant and $m$ is the cone angle parameter. Hess and Faulkner [24] give the tabulated values of $m$ for various values of the half angle $\gamma$.

As was done previously in Chapter 2 with the wedge, the given system of equations is more convenient to solve if it is transformed into a non-similar dimensionless form which can be studied as an initial-value problem. This is done by introducing the stream function: $u = \partial\psi / \partial y$, $v = -\partial\psi / \partial x$ and the variables

$$\eta = \frac{y}{x}(Pe_x^{1/2})\chi^{-1},\ \chi = \left(1+\left(\frac{Ra_x}{Pe_x}\right)^{1/2}\right)^{-1}\ \psi = \alpha(Pe_x^{1/2})\chi^{-1}S(\chi,\eta),\ \theta = \frac{T-T_\infty}{T_w-T_\infty},$$

$$f = \frac{\phi-\phi_\infty}{\phi_w-\phi_\infty},\ Pe_x = U_\infty x/\alpha,\ Ra_x = \{(1-\phi_\infty)\rho_{f\infty}g\beta_T K(T_w-T_\infty)x/\mu\alpha\}, \tag{6}$$

where $Pe_x$ is the local Peclet number, $Ra_x$ is the modified Rayleigh number, $a$ is the free stream velocity constant, and $m$ is the free stream velocity exponent. Using the expressions above one can transform equations (1) - (4) and the boundary conditions (5) into

$$S'' = (1-\chi)^2(\theta' - Nrf'), \tag{7}$$

$$\begin{aligned}&\theta'' + \frac{1}{2}(3+m\chi)S\theta' + Nbf'\theta' + Nt\theta'^2\\ &+\frac{4R_d}{3}\{\theta'\left[(H-1)\theta+1\right]^3\}' = \frac{m}{2}\chi(1-\chi)\left(S'\frac{\partial\theta}{\partial\chi} - \theta'\frac{\partial S}{\partial\chi}\right),\end{aligned} \tag{8}$$

$$f'' + \frac{Le}{2}(3+m\chi)Sf' + \frac{Nt}{Nb}\theta'' = \frac{Le}{2}m\chi(1-\chi)\left(S'\frac{\partial f}{\partial\chi} - f'\frac{\partial S}{\partial\chi}\right), \tag{9}$$

$$(3+m\chi)S(\chi,0) + m\chi(1-\chi)\frac{\partial S(\chi,0)}{\partial\chi} = 0,\ \theta(\chi,0) = 1,\ f(\chi,0) = 1 \tag{10a}$$

$$S'(\chi,\infty) = \chi^2,\ \theta(\chi,\infty) = 0,\quad f(\chi,\infty) = 0, \tag{10b}$$

where $Le = \dfrac{\alpha}{D_B}$, $Nr = \dfrac{(\rho_p - \rho_{f\infty})(\phi_w - \phi_\infty)}{(1-\phi_\infty)\rho_{f\infty}\beta(T_w - T_\infty)}$, $Nb = \dfrac{\varepsilon(\rho c)_p D_B(\phi_w - \phi_\infty)}{(\rho c)_f \alpha}$,

$$Nt = \frac{\varepsilon(\rho c)_p D_T (T_w - T_\infty)}{(\rho c)_f \alpha T_\infty}, R_d = 4\sigma T_\infty^3 / \left[k\left(a_r + \sigma_s\right)\right], H = T_w / T_\infty \ , \tag{11}$$

are the Lewis number, buoyancy ratio, Brownian motion parameter, thermophoresis parameter, conduction-radiation parameter and the surface temperature excess ratio, respectively.

### 3.3 Numerical Methods

Once again, the equations (7), (8), and (9) along with the mixed boundary conditions (10) were solved numerically using the Keller box method. The computations were again carried out with $\Delta\chi$ = 0.01 and $\Delta\eta$ = 0.01 (uniform grids), and it was found that a value of $\eta_\infty$ = 50 was sufficient enough to obtain a desired accuracy of $|\theta'(0)| < 10^{-5}$. The buoyancy ratio $N_r$, the Brownian motion parameter $N_b$, the thermophoresis parameter $N_t$, and the radiation-conduction parameter $R_d$ were first set to zero in order to compare results to those published by Yih [25]. There was an excellent agreement, and these results are presented in Table 3.1.

**Table 0.1**
**Comparison of Results with Published Results for the Full Range of Convection**

| | Yih [25] | | | Present results | | |
|---|---|---|---|---|---|---|
| $\chi$ | $m$=0.0316314 | $m$=0.2450773 | $m$=0.6667277 | $m$=0.0316314 | $m$=0.2450773 | $m$=0.6667277 |
| 0.0 | 1.0380 | 1.0380 | 1.0380 | 1.0380 | 1.0380 | 1.0380 |
| 0.1 | 0.9438 | 0.9444 | 0.9452 | 0.9438 | 0.9444 | 0.9452 |
| 0.2 | 0.8728 | 0.8751 | 0.8788 | 0.8728 | 0.8751 | 0.8788 |
| 0.3 | 0.8301 | 0.8357 | 0.8449 | 0.8301 | 0.8357 | 0.8449 |
| 0.4 | 0.8196 | 0.8301 | 0.8480 | 0.8196 | 0.8301 | 0.8480 |
| 0.5 | 0.8423 | 0.8589 | 0.8883 | 0.8423 | 0.8589 | 0.8883 |
| 0.6 | 0.8960 | 0.9191 | 0.9614 | 0.8960 | 0.9192 | 0.9615 |
| 0.7 | 0.9758 | 1.0054 | 1.0604 | 0.9758 | 1.0054 | 1.0605 |
| 0.8 | 1.0761 | 1.1117 | 1.1783 | 1.0761 | 1.1117 | 1.1784 |
| 0.9 | 1.1919 | 1.2328 | 1.3097 | 1.1920 | 1.2329 | 1.3097 |
| 1.0 | 1.3192 | 1.3648 | 1.4508 | 1.3193 | 1.3649 | 1.4509 |

Computations were also carried out for several different values of various physical parameters. The effects of these variations were examined against the dimensionless Nusselt and Sherwood numbers. Figures 3.2 and 3.3 show results for varying the cone angle parameter *m.* In these figures, $R_d = 2$, $H = 1.5$, $N_r = 0.5$, $N_b = 0.3$, $N_t = 0.1$, and $Le = 10$.

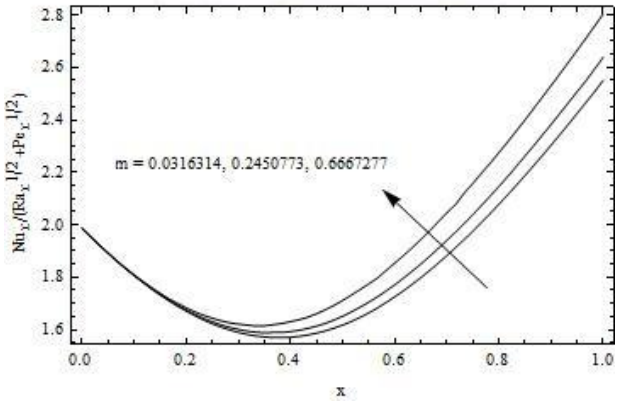


**Figure 0.2**
**The Local Nusselt Number Profile for Various Values of *m***

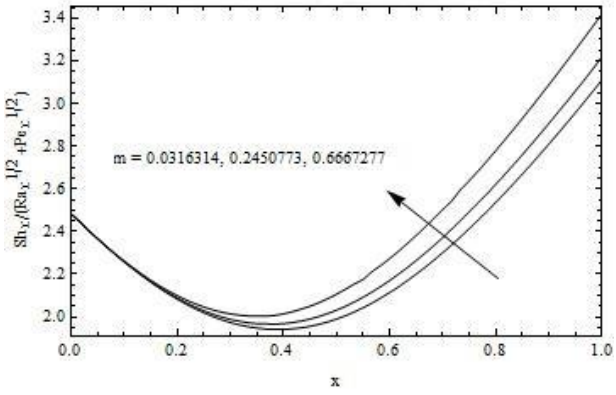


**Figure 0.3**
**The Local Sherwood Number Profile for Various Values of *m***

Figures 3.4 and 3.5 show how the local Nusselt and Sherwood numbers are affected when varying the Brownian motion parameter $N_b$. In these cases, $R_d$ = 2, $m$ = .1156458, $H$ = 1.5, $N_r$ = 0.5, $N_t$ = 0.1, and $Le$ = 10.

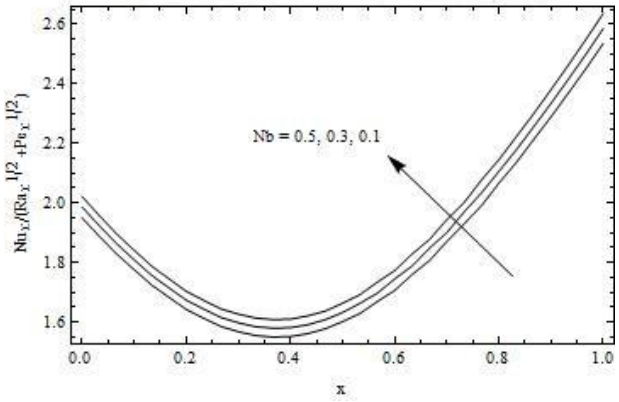


**Figure 0.4**
**The Local Nusselt Number Profile for Various Values of $N_b$**

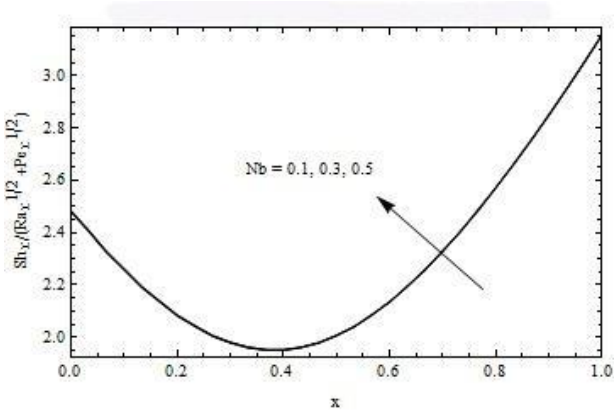


**Figure 0.5**
**The Local Sherwood Number Profile for Various Values of $N_b$**

Figures 3.6 and 3.7 show the effects of varying the thermophoresis parameter $N_t$ on the local Nusselt and Sherwood numbers. For these cases, $R_d$ = 2, $m$ = .1156458, $H$ = 1.5, $N_r$ = 0.5, $N_b$ = 0.3, and $Le$ = 10.

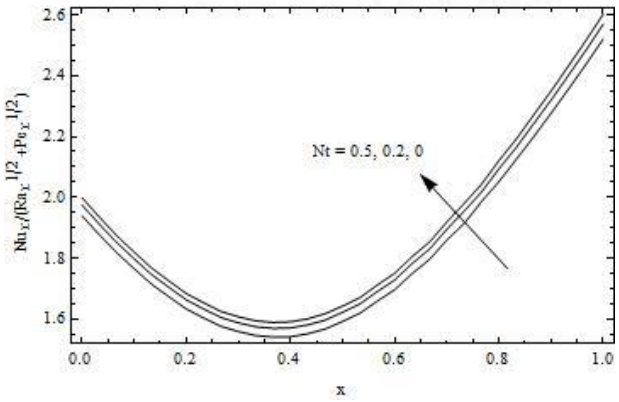


**Figure 0.6**
**The Local Nusselt Number Profile for Various Values of $N_t$**

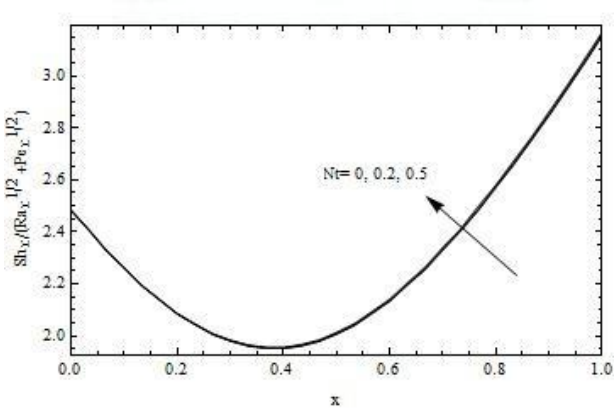


**Figure 0.7**
**The Local Sherwood Number Profile for Various Values of $N_t$**

Finally, figures 3.8 and 3.9 show the results for the radiation–conduction parameter $R_d$. In these scenarios, $m$ = .0316314, $H$ = 1.5, $N_r$ = 0.5, $N_b$ = 0.3, $N_t$ = 0.1, and $Le$ = 10.

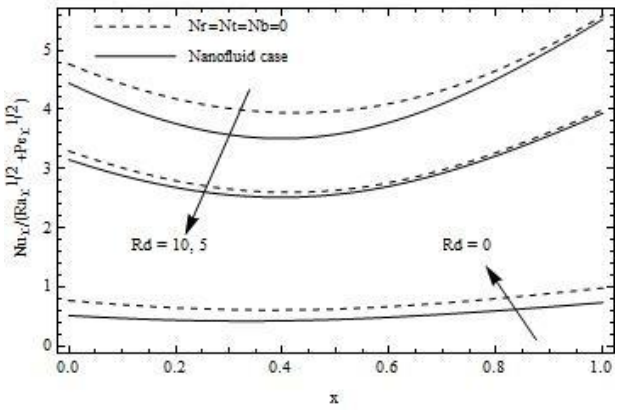


**Figure 0.8**
**The Local Nusselt Number Profile for Various Values of $R_d$**

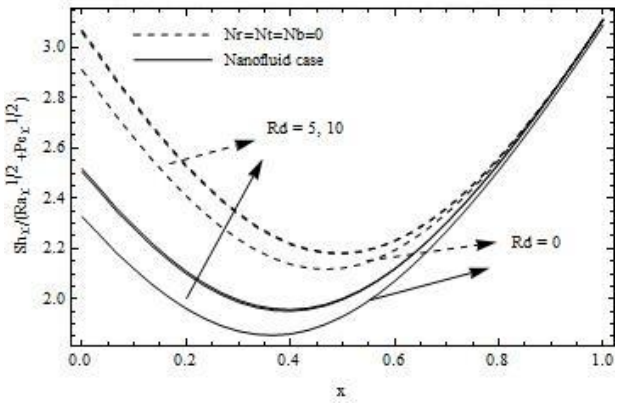


**Figure 0.9**
**The Local Sherwood Number Profile for Various Values of $R_d$**

### 3.4 Discussion of Results

Figures 3.2 and 3.3 illustrate the effects of the cone angle parameter *m* on the local Nusselt number and on the local Sherwood number in the entire range for the mixed convection parameter $(0 \le \chi \le 1)$. Note that higher values of *m* correspond to higher values of the half cone angle $\gamma$ and vice versa. From the figures one can see that increasing *m* causes both the local Nusselt and local Sherwood numbers to increase, indicating enhancements in both the heat and

mass transfer. This is true for the entire range $0 < \chi < 1$. However, it is interesting to note that the effect of *m* on the local Nusselt and local Sherwood numbers is almost negligible for pure free convection ($\chi = 0$).

Figures 3.4 and 3.5 display the changes in the local Nusselt number and local Sherwood number for various values of the Brownian motion parameter $N_b$ for the entire range of the mixed convection parameter $0 \le \chi \le 1$. It is seen that as $N_b$ increases both the local Nusselt number and local Sherwood number also increase, although the effect on the local Sherwood number is much smaller.

Figures 3.6 and 3.7 show the influence of the thermophoresis parameter $N_t$ on the local Nusselt number and local Sherwood number, respectively. Once again, results are displayed over the entire range of the mixed convection parameter $0 \le \chi \le 1$. It can be seen that increasing $N_t$ causes the local Nusselt and local Sherwood numbers to increase as well.

Figures 3.8 and 3.9 show the effect of the radiation-conduction parameter $R_d$ on the local Nusselt and local Sherwood numbers for both cases of Newtonian and nanofluids in the entire range of the mixed convection parameter $0 \le \chi \le 1$, respectively. Similar to what was seen for the wedge in Chapter 2, when $\chi = 0$ (pure free convection), it is apparent that increasing $R_d$ causes both the local Nusselt and local Sherwood number to increase. It is also seen that the local Nusselt number is more affected by $R_d$ than the local Sherwood number, which can be attributed to the fact that the local Nusselt number is more sensitive to $R_d$ and the surface temperature excess ratio *H*. Figure 3.9 also shows that as $\chi$ approaches 1 (representing pure

forced convection), the flow becomes uncoupled from the thermal and volume fraction buoyancy effects, and hence the local Sherwood number no longer depends on $R_d$.

Overall, it was observed that the local Nusselt number was found to increase whenever the half cone angle, Brownian motion, thermophoresis, or radiation-conduction parameters were increased. The local Sherwood number also increased as the half cone angle, Brownian motion, and radiation-conduction parameters were increased, but it was seen to decrease when the thermophoresis parameter was increased. It was also noticed that the local Nusselt number and local Sherwood number tended to decrease initially when moving away from pure free convection, but they eventually reached minimum values somewhere in the mixed convection area and gradually increased on the way to pure forced convection. These results were similar to what was seen with the wedge in Chapter 2. Finally, it was also observed that the effects of the radiation-conduction parameter were much stronger on the local Nusselt number than on the local Sherwood number. However, the effects of the thermophoresis parameter were actually much stronger for the local Sherwood number than the local Nusselt number.

# CHAPTER 4
# PROSPECTS FOR FUTURE WORK

The equations presented in this thesis were mathematically derived, and results were obtained numerically. A natural extension to this would therefore be for scientists to set up models similar to these problem specifications in the lab and to compare their results with those seen here. This type of work would hopefully align with the presented results and lend credence to the conclusions reached.

The system of equations also only considered two-dimensional, laminar, steady (time-independent), incompressible flow. Hence, it could be extended to include many combinations of various types of flows. For instance, many real-world applications may require a three-dimensional analysis of the flow. Several other scenarios may involve flows that are turbulent or flows that vary over time (unsteady). Finally, it was also assumed that the porous media were uniform, isotropic, and in local thermal equilibrium with the fluid. Solutions would likely be desired when some or all of those characteristics were varied.

# REFERENCES


1. Fox RW, McDonald AT. Introduction to Fluid Mechanics. 4th ed. New York: J. Wiley; 1992.

2. Schlichting H. Boundary-Layer Theory. 7th ed. New York: McGraw-Hill; 1979.

3. Pop I I, Ingham DB. Convective Heat Transfer: Mathematical and Computational Modelling of Viscous Fluids and Porous Media. 1st ed. Amsterdam: Pergamon; 2001.

4. Masuda H, Ebata A, Teramae K, Hishinuma N. Alteration of Thermal Conductivity and Viscosity of Liquid by Dispersing Ultra-Fine Particles (Dispersion of $\gamma$-$Al_2O_3$, $SiO_2$, and $TiO_2$ Ultra-Fine Particles). Netsu Bussei. 1993; 4(4):227–233.

5. Lee S, Choi SUS, Li S, Eastman JA. Measuring Thermal Conductivity of Fluids Containing Oxide Nanoparticles. ASME Journal of Heat Transfer. 1999 May; 121(2):280–288.

6. Hong KS, Hong T-K, Yang H-S. Thermal conductivity of Fe nanofluids depending on the cluster size of nanoparticles. Applied Physics Letters. 2006 January; 88(3):1–3.

7. Chopkar M, Das PK, Manna I. Synthesis and characterization of nanofluid for advanced heat transfer applications. Scripta Materialia. 2006 September. 55(6):549–552.

8. Li CH, Peterson GP. Experimental investigation of temperature and volume fraction variations on the effective thermal conductivity of nanoparticle suspensions (nanofluids). Journal of Applied Physics. 2006 May. 99(8):1–8.

9. Li CH, Williams W, Buongiorno J, Hu LW, Peterson GP. Transient and Steady-State Experimental Comparison Study of Effective Thermal Conductivity of $Al_2O_3$/Water Nanofluids. Journal of Heat Transfer. 2008 April. 130(4):042407.

10. Xuan Y, Li Q, Hu W. Aggregation structure and thermal conductivity of nanofluids. AIChE Journal. 2004 April. 49(4):1038–1043.

11. Takhar HS, Chamkha AJ, Nath G. Effect of thermophysical quantities on the natural convection flow of gases over a vertical cone. International Journal of Engineering Science. 2004 February. 42(3-4):243-256.

12. Alam MM, Alim MA, Chowdhury MMK. Free Convection from a Vertical Permeable Circular Cone with Pressure Work and Non-Uniform Surface Temperature. Nonlinear Analysis: Modelling and Control. 2007 January. 12(1):21–32.

13. Pop I, Grosan T, Kumari M. Mixed convection along a vertical cone for fluids of any Prandtl number: case of constant wall temperature. International Journal of Numerical Methods for Heat & Fluid Flow. 2003 September. 13(7):815–829.

14. Vajravelu K, Nayfeh J. Hydromagnetic convection at a cone and a wedge. International Communications in Heat and Mass Transfer. 1992 September. 19(5):701–710.

15. Chamkha AJ, Gorla RSR, Ghodeswar K. Non-similar Solution for Natural Convective Boundary Layer Flow Over a Sphere Embedded in a Porous Medium Saturated with a Nanofluid. Transport in Porous Media. 2010 June. 86(1):13-22.

16. Gorla RSR, Chamkha AJ, Rashad AM. Mixed convective boundary layer flow over a vertical wedge embedded in a porous medium saturated with a nanofluid: Natural Convection Dominated Regime. Nanoscale Research Letters. 2011 May. 6(1):207-216.

17. Bakier AY. Thermal radiation effect of mixed convection from vertical surfaces in saturated porous media. International Communications in Heat and Mass Transfer. 2001 January. 28(1):119-126.

18. Kumari M, Nath G. Radiation effect on mixed convection from a horizontal surface in a porous medium. Mechanics Research Communications. 2004 July. 31(4):483-491.

19. Yih KA. Radiation Effect on Mixed Convection over an Isothermal Wedge in Porous Media: The Entire Regime. Heat Transfer Engineering. 2001. 22(3):26-32.

20. Chamkha AJ, Abbasbandy S, Rashad AM, Vajravelu K. Radiation Effects on Mixed Convection over a Wedge Embedded in a Porous Medium Filled with a Nanofluid. Transport in Porous Media. 2012 January. 91(1):261–279.

21. Cebeci T, Bradshaw P. Physical and Computational Aspects of Convective Heat Transfer. 2nd ed. New York: Springer-Verlag; 1984.

22. Hsieh JC, Chen TS, Armaly BF. Mixed convection along a nonisothermal vertical flat plate embedded in a porous medium: The entire regime. International Journal of Heat and Mass Transfer. 1993 May. 36(7):1819-1825.

23. Chamkha AJ, Abbasbandy S, Rashad AM, Vajravelu K. Radiation Effects on Mixed Convection about a Cone Embedded in a Porous Medium Filled with a Nanofluid. Sent for Publication.

24. Hess JL, Faulkner S. Accurate values of the exponent governing potential flow about semi-infinite cone. AIAA Journal. 1965. 3:767-774.

25. Yih KA. Radiation effect on mixed convection over an isothermal cone in porous media. Heat and Mass Transfer. 2001. 37(1):53-57.